Chemical Engineering Journal 434 (2022) 134487

Contents lists available at ScienceDirect

Chemical Engineering Journal

journal homepage: www.elsevier.com/locate/cej

# Flame stand-off effects on propagation of 3D printed 94 wt% nanosized pyrolants loading composites

Haiyang Wang [a], Prithwish Biswas [a], Dylan J. Kline [a,b], Michael R. Zachariah [a,*]

[a] Department of Chemical and Environmental Engineering, University of California, Riverside, CA 92521, United States
[b] Department of Chemical and Biomolecular Engineering, University of Maryland, College Park, MD 20742, United States

ARTICLE INFO

*Keywords:*
Heat flux
Titanium
Microscopic combustion
3D printing
Biocidal

ABSTRACT

Understanding the relationship between heat transport mechanisms, particularly given the new opportunities to microstructure architecture through additive manufacturing to adjust heat flux (energy release rate per area, unit $W/m^2$), is highly desirable. In this study, we directly write free-standing iodized pyrolant sticks (94 wt% pre-assembled $Ti/Ca(IO_3)_2$ nanocomposites) with only 6 wt% binder addition. Compared to the substrate-supported pyrolant composites without using polymer (100 wt% $Ti/Ca(IO_3)_2$), we saw a > 4X reduction on the heat release rate with only 6 wt% polymer. Additionally the physically mixed case (94 wt% physically mixed $Ti/Ca(IO_3)_2$ has another 4X lower heat release rate than the above pre-assembled case. To explore heat feedback we observed the flame stand-off particularly in the samples with 6 wt% polymer via a microscopic imaging system with pyrometry. We found that with the pre-assembled and physically mixed pyrolants, the flame stand-off distances are ~ 0.7 mm and ~ 1.2 mm, respectively, which provides low heat feedback to the burning surface leading to partial ignition of nanocomposites on the burning surface. A simple thermal calculation was used to explain the relative role of the different modes of heat feedback and their relationship to stand-off and ignition.

## 1. Introduction

Pyrolant composites that incorporate metal iodates (such as $Ca(IO_3)_2$, $Cu(IO_3)_2$, $Bi(IO_3)_3$, and $AgIO_3$) have been found to have high energy densities, high adiabatic flame temperatures, and relatively high iodine content, thus making them potential candidates for efficient neutralization of biological warfare agents such as Bacillus anthracis (anthrax) spores [1–9]. However, a significant amount of the biocidal iodine released in metal iodate-based pyrolant reactions is tied up in metal iodide composites such as $CuI_2$, $BiI_3$, and AgI [2,5,10]. Fortunately, $Ca(IO_3)_2$ based pyrolant composites could maximize the release of iodine gas since the formation of CaO is greatly favored over that of $CaI_2$, and experimental results confirm that CaO is the dominant combustion product [5,11–15]. In previous studies, to better control the heat and iodine release rate of the pyrolant composites, sub-micron $Ca(IO_3)_2$ particles (0.2–1 μm) were synthesized by mechanochemistry methods, and their combustion performance was analyzed for mixtures with different metal fuels (Al, B, and Ti) [11,14–17]. Amongst them, Ti nanoparticles were found to be the most efficient to promote the decomposition of $Ca(IO_3)_2$ (anhydrous), and significantly lowered the oxygen and iodine release temperature from 660 °C to 400 °C. Consequently, the Ti case also has the lowest ignition temperature (400 °C) [15].

Composite particles alone are not bound well enough to maintain a free-standing structure without using some type of binder. However, the addition of polymer will inevitably hinder combustion performance. To achieve high energy and iodine release of $Ti/Ca(IO_3)_2$ and still maintain its mechanical integrity one needs to identify a manufacturing method that maximizes the particle loading in the composite. We have previously developed a polymer hybrid ink strategy with a mixture of hydroxy propyl methyl cellulose (HPMC) and polyvinylidene fluoride (PVDF) in which we could adhere 90 wt% Al/CuO nanothermites with 3D architectures by using only 10 wt% of polymer content [18].

In this study, we produced free-standing iodized pyrolant sticks with 94 wt% $Ti/Ca(IO_3)_2$ nanoparticle loading and only 6 % polymer addition (binder mixture). We first studied the effects of polymer addition on the combustion performance of the pyrolant composites and found only 6 % (by mass, same below) polymer could reduce the heat flux by 4-16X. We also compared the two different pyrolant sticks (both have 6% polymer content) – one is constructed by pre-assembled nano-pyrolant composites while the other is randomly packed (physically mixed with the binder mixture). The results show that the heat flux of the pre-

* Corresponding author.
*E-mail address:* mrz@engr.ucr.edu (M.R. Zachariah).

https://doi.org/10.1016/j.cej.2021.134487
Received 19 October 2021; Received in revised form 6 December 2021; Accepted 31 December 2021
Available online 5 January 2022

assembled case is 4x higher than those physically mixed. Further investigations at the microscopic scale (μm) reveal that both polymer addition and mixing conditions significantly affected the flame structure and heat feedback, via flame stand-off from the burning surface. A simple thermal calculation is shown to be consistent with the microscopic observations. Possible approaches that could reduce/prevent the flame stand-off are proposed at the end of this paper.

## 2. Experimental

### 2.1. Chemicals

Titanium nanoparticles (Ti NPs, ~50 nm, 75 wt% active Ti) were purchased from US Research Nanomaterials, Inc. Their active content was confirmed by thermogravimetric analysis (TGA). $Ca(NO_3)_2{\cdot}4H_2O$ (>99.0 %) and $KIO_3$ (99.5%) were purchased from Sigma-Aldrich. METHOCEL™ F4M Hydroxypropyl Methylcellulose (HPMC) and Polyvinylidene Fluoride (PVDF, average molecular weight: ~534,000) were obtained from Dow Chemical Company and Sigma-Aldrich, respectively. N, N dimethylformamide (DMF, 99.8%) was purchased from Sigma-Aldrich and used as a solvent to dissolve the above polymers.

### 2.2. Preparation of $Ca(IO_3)_2{\cdot}H_2O$ nanoparticles

We have previously reported a synthesis method to produce submicron and micron calcium iodate (200 nm and 2 μm) by a simple mechanochemistry method [11,15]. The details of the previous experimental condition can be found in Wang et al.[11] In this study, we modified the milling process so that we could obtain nano-sized $Ca(IO_3)_2$ particles with a diameter of 50–100 nm (Figure S1); 2–4 times smaller than those previously reported (~200 nm). To obtain nanosized $Ca(IO_3)_2$, a ball-reactant ratio of ~ 6 was loaded into a centrifuge tube (2 mL, inner diameter 9 mm, length 40 mm, purchased from Fisher Brand) as the milling container, for a Restsch CryoMill milling system operating at 25 Hz for 20 min. In a typical experiment, 1 mmol of $Ca(NO_3){\cdot}4H_2O$ and 2 mmol of $KIO_3$ were weighed into the centrifuge tube, along with 3 milling balls (Hardened steel balls, 7/32'' in diameter) and 0.5 mL ethanol. After milling, the resulting slurry was transferred to a glass vial with 10 mL ethanol and ultra-sonicated for 30 min. The obtained precipitate was centrifuged, separated, and then washed in DI water (12 mL) thrice, and ethanol (12 mL) once. The resulting white powder was dried in a vacuum oven at ~ 100 °C for 3 h and left in vacuum overnight to completely dry. The final obtained white powders were broken into loose powder and stored in an oven (~60 °C) to avoid absorbing moisture in air, and used for ink preparation and other characterizations without any other processing. The average yield is > 75%. SEM images of the obtained calcium iodates are shown in Figure S1c and S1d, and confirmed to be $Ca(IO_3)_2{\cdot}H_2O$ by X-Ray Powder Diffraction (XRD).

### 2.3. Preparation of pre-assembled (AS) pyrolant composite powder

The stoichiometric weight percentage of Ti and $Ca(IO_3)_2{\cdot}H_2O$ is 28 wt% and 72 wt%, respectively, according to Equation (1), which also considers the active content of Ti is ~ 75 wt% (crystal water was not considered when balancing Equation (1)). The obtained $Ca(IO_3)_2{\cdot}H_2O$ and Ti NPs were dispersed in hexane (10 mL) and ultra-sonicated for 30 min and dried overnight for further ink preparation and characterization.

Equation (1) is consistent with the XRD confirmed formation of $CaTiO_3$ in the combustion products (Figure S2).

$$5Ti + 2Ca(IO_3)_2 = 3TiO_2 + 2CaTiO_3 + 2I_2 \quad (1)$$

### 2.4. TGA/DSC, SEM/EDS and XRD

The thermal decomposition properties of $Ca(IO_3)_2{\cdot}H_2O$ and Ti/Ca

**Table 1**
Three different ink formulations with different polymer additions and mixing conditions.

| Materials | 0% polymer | AS-6% polymer | PM-6% polymer |
|---|---|---|---|
| Ti (mg) | 140 | 0 | 548 |
| $Ca(IO_3)_2{\cdot}H_2O$ (mg) | 360 | 0 | 1410 |
| Pre-assembled Ti/$Ca(IO_3)_2{\cdot}H_2O$ (mg) | 0 | 1958 | 0 |
| HPMC (mg) | 0 | 75 | 75 |
| PVDF (mg) | 0 | 50 | 50 |
| DMF (mL) | 0 | 4 | 4 |
| Ethanol (mL) | 2.5 | 0 | 0 |

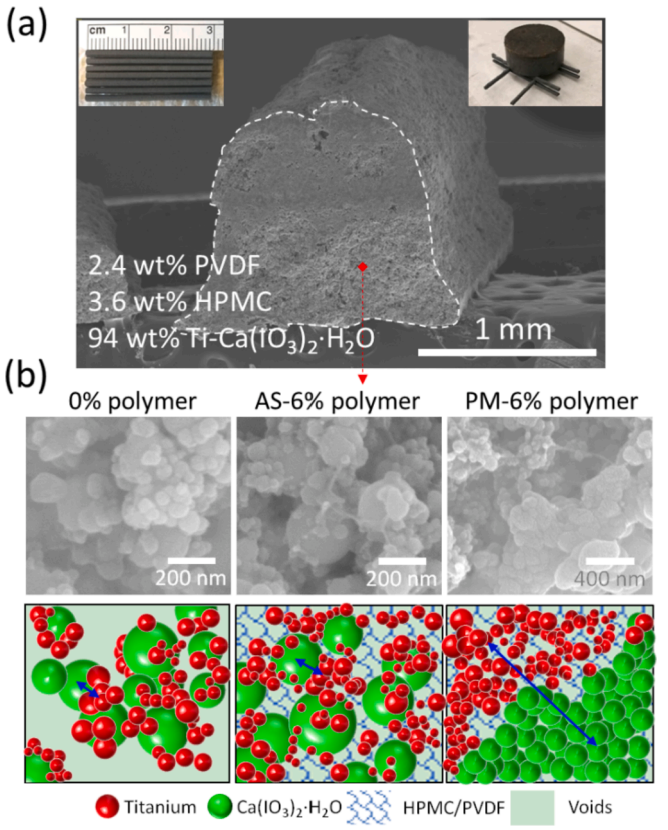


**Fig. 1.** SEM images (a) of 3D printed stick with a loading of 94 wt% pre-assembled Ti/$Ca(IO_3)_2{\cdot}H_2O$; the left insert is the optical image of the printed sticks (3 cm long); the right insert indicates the mechanical integrity of the sticks under a load (25 g); High resolution SEM images and schematic cartoon images (b) of 100 wt% Ti/$Ca(IO_3)_2{\cdot}H_2O$, 94 wt% pre-assembled and physically-mixed Ti/$Ca(IO_3)_2{\cdot}H_2O$.

$(IO_3)_2{\cdot}H_2O$, and active content of Ti NPs were characterized by a thermogravimetric analysis/differential thermal analysis (TGA/DSC) in argon (50 mL/min) and oxygen (50 mL/min), respectively, at a heating rate of 10 °C/min from room temperature to 1000 °C. The morphologies and compositions of the 3D-printed composites and combustion residues were characterized by scanning electron microscope (SEM, ThermoFisher Scientific NNS450) coupled with energy dispersive X-ray spectroscopy (EDS). The crystal structures of the synthesized $Ca(IO_3)_2{\cdot}H_2O$ and pre-assembled Ti/$Ca(IO_3)_2{\cdot}H_2O$ were characterized by X-Ray Powder Diffraction (XRD, PANalytical Empyrean Series 2) and the results were shown in Figure S3.

### 2.5. Ink preparation and direct ink writing of $Ti/Ca(IO_3)_2{\cdot}H_2O$ composites

Three different inks were prepared which correspond to three different composite films with different polymer additions and mixing conditions. The details of each ink formulation are summarized in Table 1.

We began by printing two different free-standing pyrolant sticks with a fixed polymer content of 6 wt%. In particular, 3.6 wt% HPMC and 2.4 wt% PVDF were dissolved in DMF to form a clear viscous solution. For the two different configurations with polymer, one was loaded with 94 wt% pre-assembled (AS) pyrolant composite powder (AS-6% polymer), and the other was loaded with the same total amount of powders (94 wt %) but were randomly packed in the ink (PM-6% polymer). For the former case, the pre-assembled composite powders (AS-6% polymer) were added into the above polymer solution to form a slurry, while for the latter case, Ti NPs were added first in the clear solution and then followed by the stoichiometric $Ca(IO_3)_2{\cdot}H_2O$ NPs (PM-6% polymer) to make a slurry. The slurries then underwent the same mechanical stirring for 1.5 h to achieve homogenization. Once these steps above are completed, the inks were ready for printing.

In the printing process, the inks were extruded through a 16-gauge nozzle (4.5 mL/h) and printed into pre-patterned (8 cm × 8 cm square) lines on a pre-heated substrate kept at ~ 75 °C. The printing speed (moving speed of the nozzle) was 22 cm/min. During printing we ensured that each layer was dry before depositing another layer and the resulting lines (15 layers) formed a square 8 cm × 8 cm frame with a thickness of ~ 1 mm and width of ~ 1 mm (Fig. 1). After printing, the samples were left on the heated substrate (kept at ~ 75 °C) for 30 mins to ensure evaporation of any remaining solvent. Finally, the frame was cut into 1.5 cm long sticks for combustion characterizations (Fig. 1). The porosity of the sticks (1-actual density/theoretical density) was estimated as ~ 65 % by volume [18] based on a density (mass/volume) determined from the mass divided by the volume (cross-sectional area × length of each stick) of each stick. The optical photos and cross-sectional SEM images of the sticks are shown in Fig. 1.

For the 100 wt% case, stoichiometric Ti and $Ca(IO_3)_2{\cdot}H_2O$ particles were dispersed in ethanol (particle concentration of 250 mg/mL) by ultra-sonication for ~ 1 h, after which the ink was ready for printing on glass slides. The substrate temperature was set at ~ 40 °C due to the lower boiling point of ethanol (78 °C). The porosity of the composite film was assumed to be ~ 65 % by volume for subsequent thermal transfer calculations [18].

### 2.6. T-Jump Ignition and time-resolved mass spectrometry (T-Jump MS)

The details of T-Jump MS can be found in our previous studies [19,20]. Typically, pyrolant composites were coated (~4 mm long) on a thin platinum filament (~10 mm long, ~76 μm in diameter) with a micropipette containing the above-prepared inks. The wire was then resistively heated to ~ 1400 K at a rate of ~ $4 \times 10^5$ $Ks^{-1}$ in a time-of-flight mass spectrometer. The ignition and subsequent combustion events were captured using a black and white high-speed camera (Phantom 12.1) at 1000 frames/s with a resolution of 128 × 64 pixels. Through the recorded temporal resistance data, the time-resolved temperature profiles of the platinum wire could be obtained. By correlating the observed ignition timestamp from the high-speed video with the temperature profile, the ignition temperature of the pyrolants could be calculated. At the same time, the high-speed time-of-flight mass spectrometer could provide time-resolved species evolution during the fast heating process.

### 2.7. Combustion cell

Both the composite powder and the printed sticks were evaluated in a ~ 20 $cm^3$ constant volume combustion cell coupled with an optical emission sensor [21]. The optical emission histories were recorded, and the burn time was calculated as the full-width half maximum of the curves. The sample mass was fixed at ~ 25 mg and the measurements were repeated in triplicate. When doing the tests with the printed sticks, the 3 cm long stick was broken into 2 mm pieces for consistency.

### 2.8. Macro and microscopic imaging of printed composites

The experimental setup used in this study is shown in Figure S4. The samples are either free-standing burn sticks (~3 cm long, ~1 mm wide, ~1 mm thick) with pre-assembled or physically mixed 94 wt% pyrolant, or powders deposited on glass slides at 100 wt% (no polymer added, ~2.2 cm long, ~2.6 mm wide, ~200 μm thick). Samples were placed between two camera systems with different magnifications which can be triggered simultaneously to get two videos for a single event for a front and back view. A macroscopic imaging high-speed camera (78 μm/pixel, Vision Research Phantom Miro M110) captures the back view at a sample rate of 7,000 frames/s (960 × 256 pixels), while a microscopic imaging system (~1.7 μm/pixel, Vision Research Phantom VEO710L coupled to Infinity Photo-Optical Model K2 DistaMax) captures the front view at a sample rate of 24,000 frames/s (512 × 512 pixels).

### 2.9. Burn rate and flame temperature of the printed composites

The linear burn rate ($\nu$) and flame temperature ($T_{flame}$) of the pyrolant were determined from the macroscopic imaging rather than the microscopic results since the former is able to resolve the entire combustion event. The macroscopic data was also used for the thermal calculations where burn rate and average flame temperature were required. The hot zone temperature was determined from the microscopic imaging results.

The details of how we obtained temperature by color pyrometry can be found in our previous studies [22,23]. Briefly, three-channel intensity (red, green, blue) ratios are extracted from a high-speed video color camera, are processed using a house-built MATLAB routine and demosaiced for the camera's Bayer filter using the built-in MATLAB algorithms. The system was calibrated with a blackbody source (Mikron M390) and the corresponding flame temperature maps were output and reported. The temperature uncertainty is estimated to be ~ 200–300 K.

## 3. Results and discussions

### 3.1. Morphologies and thermal properties

By using a polymer hybrid of PVDF (2.4 wt%) and HPMC (3.6 wt%), 94 wt% pre-assembled $Ti/Ca(IO_3)_2{\cdot}H_2O$ nano-sized pyrolants were successfully embedded into free-standing (insert in Fig. 1a) sticks via a simple direct writing approach. The optical and SEM images of the printed sticks are shown in Fig. 1**a**, which demonstrates the smoothly printed surface of the sticks, as well as the mechanical integrity of the high nanoparticle loading sticks. The cross-sectional SEM images indicate the close packing of the particles with minor voids.

The ink strategy used in this study was previously developed and reported to form a 90 wt% loading of Al/CuO nanothermite sticks [18] which we now are able to employ at even higher nanoparticle loadings (94 wt%). The porosity of the printed sticks was estimated as 65 % by volume according to our measurement (1-actual density/theoretical density) and is consistent with our previous study [18]. It should be noted that the densest packing for perfect spheres is ~ 74%, however, most of the nanoparticles form aggregates with typically found fractal dimensions, that can only achieve a density of ~ 33% [24]. Thus a ~ 65% porosity is probably essentially at the theoretical maximum [24].

For comparison, a 94 wt% of Ti NPs and $Ca(IO_3)_2{\cdot}H_2O$ NPs were also mixed physically with 6 wt% total amount of polymer hybrid (assigned a name of PM-6% polymer) and produced similar sticks by the same 3D printing process. Also, a substrate-supported 100 wt% $Ti/Ca(IO_3)_2{\cdot}H_2O$

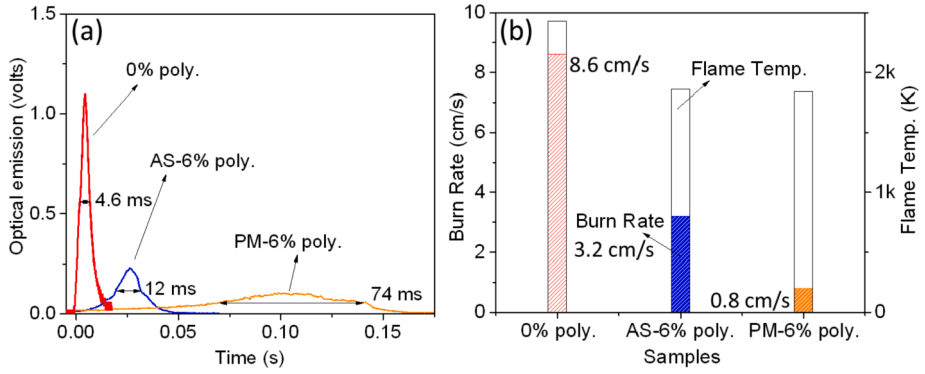


**Fig. 2.** a) Temporal optical emission from the confined combustion cell results, b) burn rate and flame temperature of 3D printed composites with different polymer addition and mixing condition from macroscopic imaging test (**0%** polymer, **AS-6%** polymer, **PM-6%** polymer).

nanocomposite films were also printed on a glass slide as the substrate to investigate the effect of polymer addition on the pyrolant (assigned a name of 0% polymer). Though no clear differences were observed between the three morphologies at low magnification (Figure S5), higher magnification SEM images (Fig. 1b) clearly show the differences caused by polymer addition and mixing conditions. As illustrated in the Fig. 1b, both 0% polymer and AS-6% polymer cases have much closer assembly between Ti NPs and $Ca(IO_3)_2{\cdot}H_2O$ NPs, yielding higher interfacial contact between fuel and oxidizer compared to PM-6% polymer case.

The estimated density, specific heat capacity, and thermal conductivity of Ti, $Ca(IO_3)_2{\cdot}H_2O$, PVDF, HPMC, and argon (filling gas in the voids) were summarized in Table S1 [25–29]. Please note that the uncertainty of the thermal conductivity estimations can be ±25%. Furthermore, the thermal diffusivity (see supporting information) and calculated burn rate of each sample were also estimated [30]. From the results listed in Table S1, we can conclude that the different composites have roughly the same thermal diffusivity (α) of ~ $1.5 \times 10^{-6}$ $m^2/s$. The ignition temperatures of different composites were also measured by our T-Jump wire ignition experiments (details can be found in Figure S6), which showed that all of the samples ignite and release $O_2/I_2$ at ~ 500 °C regardless of the polymer addition and mixing conditions. Considering the low polymer content (6 wt%) in the composites, and assuming that the primary reaction is between Ti and $Ca(IO_3)_2$ (i.e. polymer does not significantly participate in the reaction), the reaction rate (r) should remain relatively constant between all of the samples, consistent with the similar ignition events on the fast-heating wire experiments. Simple premixed flame theory [30] says that the propagation velocity is proportion to the square root of the product of the thermal diffusivity (α) and reaction rate (r) (Equation (2)). Therefore, based on Equation (2), the three different samples should burn at relatively the same rate.

$$Calculated burn rate \sqrt{\alpha \times r} \quad (2)$$

where $\alpha$ is the thermal diffusivity ($m^2/s$) and r is the reaction rate (1/s). Detailed values are summarized in Table S1 and S2.

### 3.2. Burn rate, flame temperature and heat release rate

The burn time, burn rate, and flame temperatures (Figure S7) of the three different composites with different polymer additions and mixing conditions are summarized in Fig. 2. Fig. 2a shows the optical emission histories of the samples when burned in a constant volume combustion cell where the full-width half maximum of the peak width was defined as "burn time" [21]. Clearly, the 0 % polymer case burns the fastest, with a burn time of 4.6 ms. The burn time of the AS-6% and PM-6% composites was 12 ms and 74 ms, respectively, which is 2.6x and 16x longer than the sample without polymer.

Larger, free-standing burn sticks of the composites were also evaluated in argon for their linear burn rates (was defined as total length / total burn time, total burn time was measured by a high-speed camera) and flame temperatures in a constant pressure environment (Fig. 2b). Similar to the trends seen in burn time, the linear burn rate results also

**Table 2**
Summary of parameters used to calculate the heat flux.

| Factors | 0% polymer | AS-6% polymer | PM-6% polymer |
|---|---|---|---|
| $\nu$, Linear burn rate (m/s) | 0.086 ± 0.002 | 0.032 ± 0.004 | 0.008 ± 0.001 |
| $\rho$, Density ($kg/m^3$) | 1581 | 1404 | 1404 |
| $C_P$, Specific heat capacity (J/(kg·K) | 930 | 950 | 950 |
| $T_{flame}$, Flame temperature (K) | 2430 | 1860 | 1840 |
| **G, Heat flux ($W/m^2$)** | **$2.7 \times 10^8$** | **$6.7 \times 10^7$** | **$1.6 \times 10^7$** |

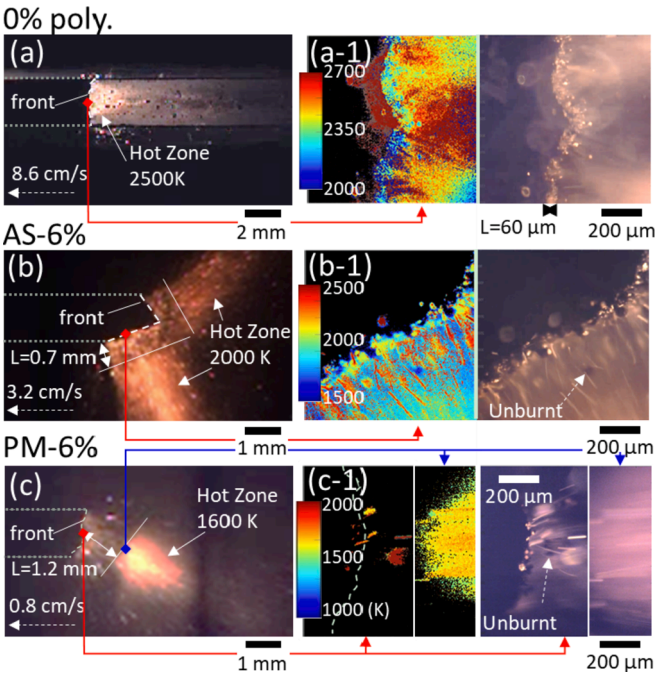


**Fig. 3.** Macroscopic (a-c) and microscopic imaging (a-1 ~ c-1) snapshots of the 3D printed composites with different polymer addition and mixing condition. (a and a-1) 100 wt% $Ti/Ca(IO_3)_2{\cdot}H_2O$, 94 wt% pre-assembled (b and b-1) and physically-mixed (c and c-1) $Ti/Ca(IO_3)_2{\cdot}H_2O$. It is notable that in c-1, the two figures have a distance of ~ 1 mm, which corresponds to the flame front and hot zone, respectively.

show the 0 % polymer case burns the fastest, at a rate of ~ 8.6 cm/s, which is 2.7 × and 11 × higher than the AS-6% polymer and PM-6% polymer cases, respectively. The flame temperature of 0% polymer also is 2430 K, which is ~ 580 K higher than the ones with 6 wt% polymers. Based on the results from measured linear burn rates and flame temperatures and combined with the physical properties data estimated in Table 2, we can estimate the heat flux [31–33] (energy release rate per area, $G$, W/m$^2$) from Equation (3). The heat flux of the 0% polymer sample is calculated to be 4x and 16x times higher than the AS-6% polymer case and the PM-6% polymer case, respectively. These results clearly are in clear contradiction to the calculation we obtained above: that the burn rates of different samples should be similar according to Equation (2). This clearly suggests that structure, something that is not described in Equation (2) is important. In fact, as we will show later, both 6 wt% polymer-containing sticks are burning differently: the flame is standing-off from the burning surfaces.

$$G = \nu \times \rho \times c_p \times \left(T_{flame} - T_{room}\right) \tag{3}$$

Where $\nu_m$ is the mass burn rate (kg/s); $\Delta T$ (K) is the difference between flame temperature ($T_{flame}$) and room temperature ($T_{room}$, 300 K).

### 3.3. Reduced heat feedback with separated flame from the burning front

As shown in the above sections, we obtained very different heat flux values with different polymer additions and mixing conditions. From the high-speed macroscopic imaging videos, in Fig. 3 we observed that the flame stands off from the burning surfaces for both cases with 6 wt% polymer, which might significantly affect the heat transfer efficiency. The flame structures of different composites were simultaneously captured by both a high-speed color camera (78 μm/pixel) and a microscopic imaging system (1.7 μm/pixel). Typical snapshots of the combustion events can be seen in are shown in Fig. 3a-3c, and Fig. 3a-1 ~ 3c-1, respectively (More details in Figure S8 and supporting information). Both of the polymer-containing samples exhibited a clear standoff distance between the burning plume and burning front, which was ~ 0.7 mm for AS-6% polymer case and ~ 1.2 mm for PM-6% polymer case. The 0% polymer sample however, did not demonstrate any such standoff behavior. Closer analysis of reaction fronts as viewed with the microscope imaging system revealed more details, where it was found that the 0% polymer samples had a thin, clearly defined reaction fronts spanning ~ 60 μm [33], whereas the polymer-containing samples did not have a well-defined reaction front.

From these images, it was clear that only a small percentage mass fraction of the surface was being successfully ignited at the bulk sticks. The large unburnt pieces of materials were stripped off from the composite sticks due to the decomposition of the binding polymers. The stripped-off unburnt materials ignited later and formed a stand-off flame with a hot zone (which we observed as a hot plume in Fig. 3, details can be seen in the supporting videos). The temperatures of the hot zones (the average temperature based on the data points in the hot zone) for each sample are also obtained and shown in Fig. 3. For 0% polymer case, the hot zone temperature is the highest as 2500 K, which is ~ 500 K and ~ 900 K higher than the AS-6% polymer and PM-6% polymer cases, respectively. Considering the separations between hot zone and burning front for the composites with 6 wt% polymer, it is not surprising that the heat feedback to the burning front is lower, which result in incomplete combustion and a lower heat release rate (4X-16X lower compared to 0% polymer case) [23,34]. Obviously, compared to the AS-6% polymer case, the PM-6% polymer case was affected even more by this phenomenon, since the stand-off distance is longer and also significantly fewer ignitions were observed in the microscopic snapshots (more details could be found in Figure S8 and supporting videos). Therefore, the PM-6% polymer case has a 4X lower heat release rate compared to the AS-6% one.

To roughly quantify the mass fractions that were ignited in the composites sticks, we performed a simple conduction and radiation heat transfer calculation that considers the influence of hot zone (plume) [23,35].

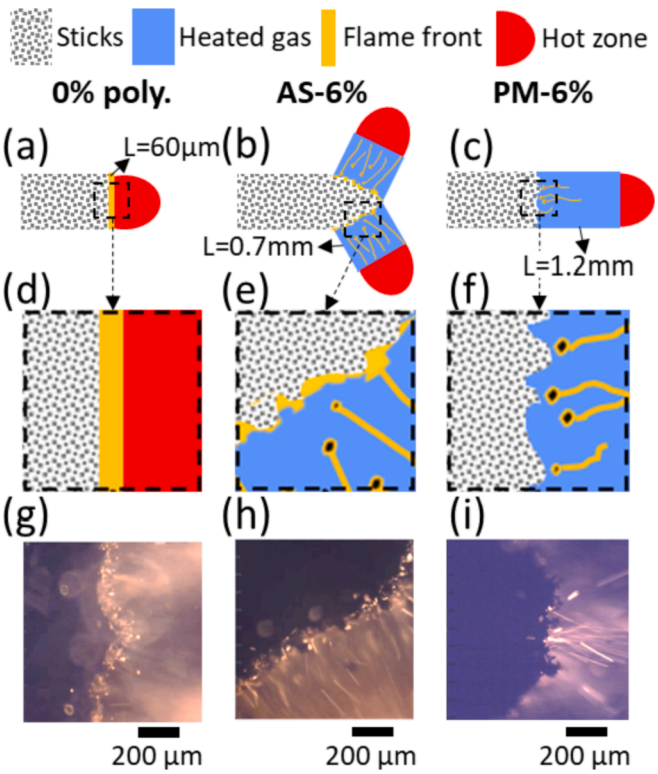


**Fig. 4.** The schematic showing (a-c) microscopic imaging snapshots of the 3D printed composites with different polymer addition and mixing condition. The zoomed-in schematic demonstrations (d-f) and microscopic imaging snapshots (g-i) of the different combustion surfaces. (a, d, g) 100 wt% Ti/$Ca(IO_3)_2{\cdot}H_2O$, (no polymer) (b, e, h) 94 wt% pre-assembled and (c, f, i) physically-mixed Ti/$Ca(IO_3)_2{\cdot}H_2O$.

### 3.4. Calculations on partial ignition on the burning front

Heat transfer modes play critical roles on the ignition and combustion of pyrolants [23,35]. In the most commonly studied Al/CuO system, the generating heat is transferred not only conduction and radiation, but also through convection, metal vapor condensation and especially hot particle advection. The latter is thought to play an even more important role on flame propagation than the heat conduction and radiation [23,35]. As for the case of Ti/$Ca(IO_3)_2$, there are very limited metal vapor condensation and particle advection since the boiling point of Ti (3560 K) is significantly higher than its flame temperature (<2500 K). $Ca(IO_3)_2$ only release iodine gas and the final products is CaO (melting point 2845 K) which also would not produce any metal vapor or droplets. The produced gas species in this study will be oxygen, iodine vapor and decomposition products coming from the polymer mixture of HPMC and PVDF. The enthalpy of condensation of iodine is 20.7 kJ/mol, which is only ~ 1/15 of Al (293.4 kJ/mol) and Cu (300.3 kJ/mol). Moreover, the polymer content is only 6 wt% and its decomposition is endothermic. Therefore, based on the above, to better compare the three, we will just consider the heat conduction and radiation to calculate the heat feedback from the hot zone to the burning surface.

The illustrations in Fig. 4a-4f demonstrate the locations of burning fronts and hot zones as observed in the microscopic imaging system. If we assume that at any given instant only some fraction of the surface is actually burning, we can make a further assumption that the fraction burning can be correlated to the amount of energy reaching the surface sufficient to the ignition criteria. Then the mass fraction (mass %)

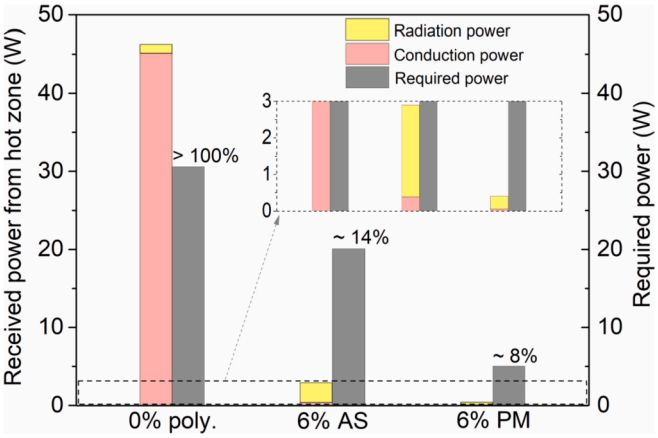


**Fig. 5.** Calculations results of the mass fraction (%) of the burning front that was ignited on the surface based on energy received from the hot zone via conduction and radiation, as well as the energy required to maintain the measured burn rates.

ignited at the reaction front is estimated based on equation (4–7) as a fraction of the energy coupled to the surface relative to that required for ignition:

$$Mass_{ign}\% = \frac{\dot{Q}_{cond} + \dot{Q}_{rad}}{\dot{Q}_{required}} \tag{4}$$

$$\dot{Q}_{cond} = kA_{burning}\frac{T_H - T_{ign.}}{L} \tag{5}$$

$$\dot{Q}_{rad} = \sigma A_{burning}\left(T_H^4 - T_{ign.}^4\right) \tag{6}$$

$$\dot{Q}_{required} = \rho \times A \times C_P \times \left(T_{ign.} - T_{ambient}\right) \times \nu \tag{7}$$

Where k is thermal conductivity of the materials between hot zone and flame front (W/m·K); *where*$\sigma$*is the* Stefan-Boltzmann constant is approximately 5.67 × $10^{-8}$ W/m.$T_H$ is the temperature of the hot zone (K); $T_{ambient}$ = 300 K; L is the distance between the hot zone and burning surface (m).$T_{ign.}$ is the ignition temperature of the composites, which is 770 K, based on our T-Jump wire ignition tests. $A_{burning}$ is the burning surface area ($m^2$). Note: the heat feedback power received from conduction ($\dot{Q}_{cond}$, W) and radiation ($\dot{Q}_{rad}$, W), as well as the energy power required ($\dot{Q}_{required}$, W) could be obtained from equations in the supporting information [35].

Fig. 5 and Table S4 summarized the calculation results of both conduction and radiation power from hot zones (more details in Supporting Information). It is clear the for 0% polymer case, the conduction power is much higher than the other two cases and also much higher than its radiation power due to the thin flame front thickness (~60 μm). Another contributor to this huge difference is the phase difference of the heat transfer media material spanning the standoff distance, which is solid composite material in the 0% polymer case as opposed to a gas species in the polymer containing cases – the solid composite can transfer heat > 50x faster via conduction than the gas [27]. It is also noted that for 6% polymer containing samples, the heating power contribution from conduction is now lower than radiation, which is to be expected since the gas effectively acts as an insulator for conductive heat transfer. If the final results show the summed power (convention and radiation) from hot zone is higher than the required power to support measured linear burn rate, there will be a 100 mass % of the cross-sectional area igniting and burning (such as the 0% poly. case). On the contrast, for AS-6% and PM-6% polymer cases, the summed power is only ~ 14% and ~ 8% of the required power, respectively, indicating only a small mass percentage of the area was successfully ignited. Again, the microscopic snapshots in Fig. 4h and 4i confirm that only partial ignition occurring on the burning fronts, and clearly the physically mixed case (~8%) is even less than the pre-assembled one (~14%).

Thus far, we have demonstrated that the hot zone temperature ($T_H$) and the distance to the burning front ($L$) are key factors that can significantly affect the energy feedback to the composite via conduction and radiation. To better demonstrate these effects, the ignited cross-sectional mass percentages were simulated by manipulating both the separation distance ($L$) and hot zone temperature ($T_H$). On the one hand, as shown in Fig. 6 for the AS-6% (hot zone ~ 2000 K) and PM-6% (hot zone ~ 1600 K) cases, the simulated ignited area (%) remains roughly

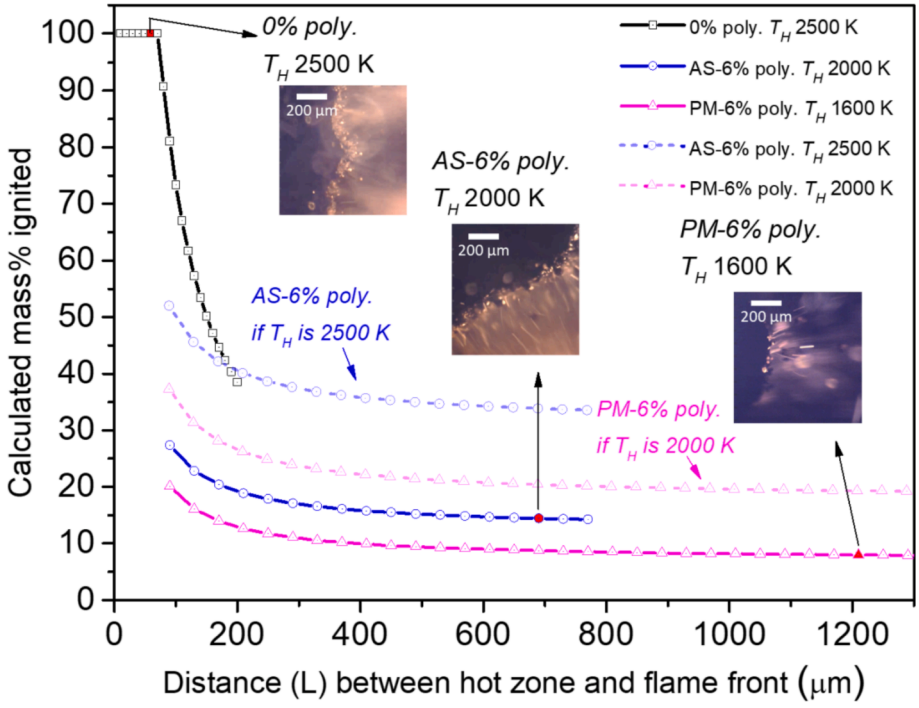


**Fig. 6.** Calculated ignited area percentage (%) changes with the distance between hot zone and burning front. The insert figures are the measured points in this work. Solid lines are at the hot zone temperatures that were obtained in this work, that is, 2500 K for 0% polymer, 2000 K for AS-6% polymer and 1600 K for PM-6% polymer case. Two more dash lines were added to see how the hot zone temperature increase (AS-6% poly. increases from 2000 K to 2500 K; PM-6% poly. increases from 1600 K to 2000 K) affecting the simulation.

constant until the distance ($L$) between hot zone and burning front was reduced to <~300 μm. The simulated ignited area (%) could be increased by 50% if the distance (L) was reduced from ~ 300 μm to ~ 130 μm. On the other hand, if we could raise the hot zone temperatures by ~ 500 K (as for AS-6% and PM-6%, hot zone temperatures increase from 2000 K to 2500 K, and from 1600 K to 2000 K, respectively), the simulated ignited area could be doubled (dashed lines). Once the hot zone temperature ($T_H$) increases to ~ 2500 K and the distance ($L$) reduces to 130 μm, the ignited area (%) becomes very sensitive to the distance ($L$), which quickly achieves 100 % area ignition if the distance ($L$) is ~ 70 μm (for 0% poly. case in Fig. 6). Once the majority of the cross-section of the composite could be successfully ignited, the flame will attach directly to the flame front, which will further highly increase the heat diffusivity by altering the heat transfer medium from gas to solid, as seen in Fig. 6 for the 0% poly. case.

Considering both flame temperature and standoff distance can manipulated based on the different manufacturing methods, implies the ability to similarly modulate the heat flux. For example, changing the composition and chemistry might alter the flame temperatures (such as incorporating Al/$WO_3$, Al/$Fe_2O_3$, etc.), while replacing the aggregated particles with more finely dispersed particles (such as pre-ball milled pyrolants) that has lower ignition temperature might significantly reduce the standoff distance.

## 4. Conclusions

In this study, we printed free-standing iodized sticks with a 94 wt% loadings of pre-assembled and physically mixed nano-sized pyrolants. We studied the effect of polymer addition on the combustion of pyrolant, and found that only 6 % polymer was sufficient to reduce the heat flux by 4X-16X. The heat flux of the pre-assembled case is 4X higher than the physically mixed sticks. Further investigation on the flame structure at a microscopic scale (μm) allowed us to observe the flame stand-off phenomenon, in which unburnt materials stripped off from the flame front and ignited ~ 1 mm away to form a hot zone, providing heat. Consequently, only a small mass fraction of the composites on the front were successfully ignited. A simple thermal calculation to estimate the mass fractions of materials that could be ignited by the hot zone via heat conduction and radiation, was used to parametrize against our microscopic observations. This study also provides some insights on the role of the polymer and mixing condition on the propagation of composites.

## Declaration of Competing Interest

The authors declare that they have no known competing financial interests or personal relationships that could have appeared to influence the work reported in this paper.

## Acknowledgments

This project is sponsored by the Department of the Defense, Defense Threat Reduction Agency under the MSEE URA, HDTRA1-20-2-0001. The content of the information does not necessarily reflect the position or the policy of the federal government, and no official endorsement should be inferred. Electron microscopy on quenched samples was performed using an FEI NNS450 SEM in the Central Facility for Advanced Microscopy and Microanalysis at the University of California, Riverside.

## Appendix A. Supplementary data

Supplementary data to this article can be found online at https://doi.org/10.1016/j.cej.2021.134487.

## References

[1] X. Hu, J.B. DeLisio, X. Li, W. Zhou, M.R. Zachariah, Direct deposit of highly reactive $Bi(IO_3)_3$-polyvinylidene fluoride biocidal energetic composite and its reactive properties, Adv. Eng. Mater. 19 (1) (2017) 1500532, https://doi.org/10.1002/adem.201500532.
[2] H. Wang, G. Jian, W. Zhou, J.B. DeLisio, V.T. Lee, M.R. Zachariah, Metal iodate-based energetic composites and their combustion and biocidal performance, ACS Appl. Mater. Interfaces 7 (31) (2015) 17363–17370, https://doi.org/10.1021/acsami.5b04589.
[3] K.S. Martirosyan, L. Wang, A. Vicent, D. Luss, Synthesis and performance of bismuth trioxide nanoparticles for high energy gas generator use, Nanotechnology 20 (40) (2009) 405609, https://doi.org/10.1088/0957-4484/20/40/405609.
[4] C.E. Johnson, K.T. Higa, Iodine-rich biocidal reactive materials, MRS Online Proceedings Library (OPL) 1521 (2013), https://doi.org/10.1557/opl.2013.46.
[5] J.C. Oxley, J.L. Smith, M.M. Porter, M.J. Yekel, J.A. Canaria, Potential biocides: iodine-producing pyrotechnics, Propellants Explos. Pyrotech. 42 (8) (2017) 960–973, https://doi.org/10.1002/prep.201700037.
[6] K.T. Sullivan, N.W. Piekiel, S. Chowdhury, C. Wu, M.R. Zachariah, C.E. Johnson, Ignition and combustion characteristics of nanoscale Al/$AgIO_3$, Combust. Sci. Technol. 3 (2010) 285–302, https://doi.org/10.1080/00102202.2010.496378.
[7] X. Hu, W. Zhou, X. Wang, T. Wu, J.B. Delisio, M.R. Zachariah, On-the-fly green generation and dispersion of AgI nanoparticles for cloud seeding nuclei, J. Nanopart. Res. 18 (2016) 1–10, https://doi.org/10.1007/s11051-016-3528-5.
[8] I. Shancita, K.K. Miller, P.D. Silverstein, J. Kalman, M.L. Pantoya, Synthesis of metal iodates from an energetic salt, RSC Adv. 10 (24) (2020) 14403–14409, https://doi.org/10.1039/D0RA02250K.
[9] D. Tang, S. Chen, X. Liu, W. He, G. Yang, P.-J. Liu, M. Gozin, Q.-L. Yan, Controlled reactivity of metastable n-Al@$Bi(IO_3)_3$ by employment of tea polyphenols as an interfacial layer, Chem. Eng. J. 381 (2020) 122747, https://doi.org/10.1016/j.cej.2019.122747.
[10] L.N. Kotter, L.J. Groven, Boron carbide based biocide compositions: a study of iodate particle size on combustion and iodine output, Propellants Explos. Pyrotech. 45 (3) (2020) 509–516, https://doi.org/10.1002/prep.201900278.
[11] H. Wang, J.B. DeLisio, T. Wu, X. Wang, M.R. Zachariah, One-step solvent-free mechanochemical synthesis of metal iodate fine powders, Powder Technol. 324 (2018) 62–68, https://doi.org/10.1016/j.powtec.2017.10.024.
[12] S. Wang, X. Liu, M. Schoenitz, E.L. Dreizin, Nanocomposite thermites with calcium iodate oxidizer, Propellants Explos. Pyrotech. 42 (3) (2017) 284–292, https://doi.org/10.1002/prep.201600213.
[13] E.M. Hunt Biocidal Energetic Materials for the Destruction of Spore Forming Bacteria, Defense Threat Reduction Agency 2015 1 47.
[14] X. Liu, A. Sims, C. Murzyn, N.G. Glumac, E.L. Dreizin, Iodine release by combustion of composite Mg•Ca(IO3)2 Powder, Combust. Sci. Technol. 193 (6) (2021) 1042–1054, https://doi.org/10.1080/00102202.2019.1680653.
[15] H. Wang, D.J. Kline, M. Rehwoldt, M.R. Zachariah, Ignition and combustion characterization of $Ca(IO_3)_2$-based pyrotechnic composites with B, Al, and Ti, Propellants Explos. Pyrotech. 43 (10) (2018) 977–985, https://doi.org/10.1002/prep.201800041.
[16] X. Liu, M. Schoenitz, E.L. Dreizin, Preparation, ignition, and combustion of magnesium-calcium iodate reactive nano-composite powders, Chem. Eng. J. 359 (2019) 955–962, https://doi.org/10.1016/j.cej.2018.11.091.
[17] X. Liu, M. Schoenitz, E.L. Dreizin, Boron-based reactive materials with high concentrations of iodine as a biocidal additive, Chem. Eng. J. 325 (2017) 495–501, https://doi.org/10.1016/j.cej.2017.05.100.
[18] H. Wang, J. Shen, D.J. Kline, N. Eckman, N.R. Agrawal, T. Wu, P. Wang, M. R. Zachariah, Direct writing of a 90 wt% particle loading nanothermite, Adv. Mater. 31 (23) (2019) 1806575, https://doi.org/10.1002/adma.201806575.
[19] L. Zhou, N. Piekiel, S. Chowdhury, M.R. Zachariah, T-Jump/time-of-flight mass spectrometry for time-resolved analysis of energetic materials, Rapid Commun. Mass Spectrom. 23 (1) (2009) 194–202, https://doi.org/10.1002/rcm.3815.
[20] J.B. DeLisio, X. Hu, T. Wu, G.C. Egan, G. Young, M.R. Zachariah, Probing the reaction mechanism of aluminum/fluoropolymer composites, J. Phys. Chem. B 120 (2016) 5534–5542, https://doi.org/10.1021/acs.jpcb.6b01100.
[21] K. Sullivan, G. Young, M.R. Zachariah, Enhanced reactivity of nano-B/Al/CuO MIC's, Combust. Flame 156 (2) (2009) 302–309, https://doi.org/10.1016/j.combustflame.2008.09.011.
[22] R.J. Jacob, D.J. Kline, M.R. Zachariah, High speed 2-dimensional temperature measurements of nanothermite composites: Probing thermal vs, Gas generation effects. J. Appl. Phys. 123 (11) (2018) 115902, https://doi.org/10.1063/1.5021890.
[23] D.J. Kline, Z. Alibay, M.C. Rehwoldt, A. Idrogo-Lam, S.G. Hamilton, P. Biswas, F. Xu, M.R. Zachariah, Experimental observation of the heat transfer mechanisms that drive propagation in additively manufactured energetic materials, Combust. Flame 215 (2020) 417–424, https://doi.org/10.1016/j.combustflame.2020.01.020.
[24] C.D. Zangmeister, J.G. Radney, L.T. Dockery, J.T. Young, X. Ma, R. You, M. R. Zachariah, Packing density of rigid aggregates is independent of scale, P. N. A. S. 111 (25) (2014) 9037–9041, https://doi.org/10.1073/pnas.1403768111.
[25] K. Zhou, H.P. Wang, J. Chang, B. Wei, Experimental study of surface tension, specific heat and thermal diffusivity of liquid and solid titanium, Chem. Phys. Lett. 639 (2015) 105–108, https://doi.org/10.1016/j.cplett.2015.09.014.
[26] C.K. Sahoo, S.R.M. Rao, M. Sudhaka, HPMC a biomedical polymer in pharmaceutical dosage forms, J. Chem Pharm. Sci. (2015) 875–881.
[27] R.W. Powell, C.Y. Ho, P.E. Liley, Thermal conductivity of selected materials, US Department of Commerce, National Bureau of Standards Washington, DC, 1966.

[28] H.J. Lee, R.E. Taylor, Thermal diffusivity of dispersed composites, J. Appl. Phys. 47 (1) (1976) 148–151, https://doi.org/10.1063/1.322335.
[29] R.C. Progelhof, J.L. Throne, R.R. Ruetsch, Methods for predicting the thermal conductivity of composite systems: A review, Polym. Eng. Sci. 16 (9) (1976) 615–625, https://doi.org/10.1002/pen.760160905.
[30] E. Mallard, H.L. Le Chatelier, Thermal model for flame propagation, Ann. Mines 18 (1883) 379–568.
[31] A.S. Mukasyan, A.S. Rogachev, Discrete reaction waves: Gasless combustion of solid powder mixtures, Prog. Energy Combust. Sci. 34 (3) (2008) 377–416, https://doi.org/10.1016/j.pecs.2007.09.002.
[32] H. Wang, D.J. Kline, M.R. Zachariah, In-operando high-speed microscopy and thermometry of reaction propagation and sintering in a nanocomposite, Nat. Commun. 1 (2019) 3032–3038, https://doi.org/10.1038/s41467-019-10843-4.
[33] H. Wang, B. Julien, D.J. Kline, Z. Alibay, M.C. Rehwoldt, C. Rossi, M.R. Zachariah, Probing the reaction front of nanolaminates at ~μs time and ~μm spatial resolution, J. Phys. Chem. C 124 (2020) 13679–13687, https://doi.org/10.1021/acs.jpcc.0c01647.
[34] D.J. Kline, M.C. Rehwoldt, H. Wang, N.E. Eckman, M.R. Zachariah, Why does adding a poor thermal conductor increase propagation rate in solid propellants? Appl. Phys. 115 (11) (2019) 114101, https://doi.org/10.1063/1.5113612.
[35] G.C. Egan, M.R. Zachariah, Commentary on the heat transfer mechanisms controlling propagation in nanothermites, Combust. Flame 162 (7) (2015) 2959–2961, https://doi.org/10.1016/j.combustflame.2015.04.013.